Chemical Engineering Science 176 (2018) 35–49

Contents lists available at ScienceDirect

Chemical Engineering Science

journal homepage: www.elsevier.com/locate/ces

Study on the meniscus-induced motion of droplets and bubbles by a three-phase Lattice Boltzmann model

Bei Wei [a,b], Haibo Huang [c], Jian Hou [a,*], Michael C. Sukop [b]

[a] State Key Laboratory of Heavy Oil Processing, China University of Petroleum, Qingdao, Shandong 266580, China
[b] Department of Earth and Environment, Florida International University, Miami, FL 33199, USA
[c] Department of Modern Mechanics, University of Science and Technology of China, Hefei, Anhui 230026, China

HIGHLIGHTS

- We study the meniscus-induced motion of droplets and bubbles by LBM.
- Symmetry and relative density of a droplet interacting with gravity influence the motion.
- Gravity may enhance the bubble motion towards the wall.

GRAPHICAL ABSTRACT

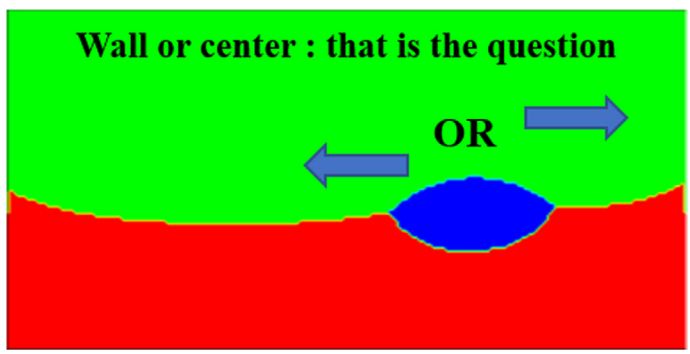

ARTICLE INFO

Article history:
Received 12 April 2017
Received in revised form 26 September 2017
Accepted 20 October 2017
Available online 21 October 2017

Keywords:
Lattice Boltzmann model
Three phase
Meniscus-induced motion
Curvatures

ABSTRACT

In contrast to typical applications of the pseudopotential Lattice Boltzmann model to two components, quantitative validations and applications for three-component Shan-Chen model are performed here. First, the qualitative and quantitative validations for the following three cases were performed, i.e., three-phase separation, meniscus-induced bubble movement, and the three-phase layered flow. A scheme to control the simulated contact angle of droplets on the interface is provided for the three fluid phase Lattice Boltzmann model. The effects of droplet shape, the strength of gravity, droplet size, and meniscus curvature for the spontaneous motion of droplets and bubbles are investigated in detail. It is found that without gravity, droplets tend to move to the wall on a concave upwards meniscus when they have a big "head" and a small "belly". Gravity may enhance rather than inhibit the motion towards the wall when the density of the droplet or bubble is relatively small. Finally, smaller droplet size and larger meniscus curvatures enhance the spontaneous movement towards a wall. The conclusions are relevant to practical applications such as water treatment, oil spill remediation, and droplet-based microfluidics.
© 2017 Elsevier Ltd. All rights reserved.

1. Introduction

Physical and chemical phenomena that occur at the interface between two phases are ubiquitous in nature, such as adsorption and desorption, wetting behaviors, interfacial reactions, and so on. Recently, a fascinating type of interfacial phenomenon, the self-propelled motion of particles, droplets, and bubbles on an interface, has aroused increasing interest in both fundamental research and industrial applications (Chen et al., 2017; Wang et al., 2016). Frequently encountered in our daily lives, the "tears of wine" phenomenon (Fournier and Cazabat, 1992), caused by

* Corresponding author.
E-mail address: houjian@upc.edu.cn (J. Hou).

https://doi.org/10.1016/j.ces.2017.10.025
0009-2509/© 2017 Elsevier Ltd. All rights reserved.

the chemical Marangoni effect, and the propensity of floating objects to aggregate, i.e., the so called "Cheerios effect" (Vella and Mahadevan, 2005), are perfect examples of such phenomena. Moreover, this spontaneous motion also plays an important role in modern technologies related to droplet-based microfluidics, deposition of pesticides on plant foliage, leaking oil collection, and many other processes.

In essence, most spontaneous motions are surface-free-energy-driven and several different driving forces have been identified. These driving forces include but are not limited to:

(1) Interfacial tension gradients at liquid-liquid and gas-liquid interfaces. The inhomogeneous interfacial tension usually results from interfacial mass transfer due to a thermal gradient or chemical concentration gradient across the interface (Oshima et al., 2014; Sumino et al., 2005; Rybalko et al., 2004; Nakata et al., 1997; Matsushita et al., 2012).
(2) Wettability gradients on solid surfaces or substrates. In fact, wettability gradients are the macroscopic manifestation of interfacial tension gradients. It is on solid surfaces exhibiting a surface energy gradient or surface roughness variation that self-propelled motions are most widely studied (Genzer, 2012; Hernandez et al., 2013; Hilner et al., 2009; Sun et al., 2008; Alheshibri et al., 2013). According to Genzer's (2012) classification, gradients on surfaces are characterized by a few key attributes, i.e., type (chemical, mechanical, and topographical), dimensionality, directionality, length scale, and time dependency.
(3) Geometrical gradients. The geometrical gradient refers specifically to curvature gradient here and could exist either on surfaces or interfaces. Lv et al., 2014 reported a driving force leading to droplet motion in which a substrate curvature gradient can accelerate micro- and nano-droplets to high speeds on both hydrophilic and hydrophobic substrates. They showed that the total free energy and driving force exerted on a droplet are determined by the substrate curvature and substrate curvature gradient, respectively. Moreover, capillary migration of microdisks on oil-water curved interfaces was reported by Yao et al. (2015). Liu and Hou's group (Li et al., 2015; Liu et al., 2016) then found that an oil droplet on the meniscus could be attracted to the wall when surfactant is added to water, while bubbles always move towards the walls; interfacial tensions and gravity play important roles in these cases.
(4) Electrostatic and magnetic force. It is not surprising that charged droplets or ferrofluid droplets move under the influence of an electric or magnetic field (Woog Lee et al., 2012; Nguyen et al., 2006). However, uncharged droplets or particles can also move under such fields due to the dielectrophoresis (DEP) phenomenon (Gascoyne et al., 2004).
(5) Multi-gradients and others. Self-propelled motion may be driven by multi-gradients in many cases (Hou et al., 2013). Undoubtedly, there are other perhaps unexpected phenomena driven by different forces, such as water skittering across a hot pan as a result of the Leidenfrost effect (Celestini et al., 2013) and the motion of an adhesive gel in a swelling gradient (Joanny et al., 2003).

The study of such phenomena is dominated by experimental work and numerical simulations are relatively rare. Previous numerical simulations primarily focus on motions on solid surfaces. The methods applied in the numerical simulations include molecular dynamics methods, traditional Computational Fluid Dynamics (CFD) methods based on solutions of the macroscopic Navier-Stokes equations and minimum-surface-energy-based solvers such as Surface Evolver (Lv et al., 2014; Xu and Qian, 2012). These simulation methods can solve many problems concerning interfacial phenomenon. However, they also have some disadvantages in that molecular dynamics methods are computationally expensive and generally limited to the nanoscale; traditional CFD methods have to be used together with a technique to track/-capture interfaces between phases when dealing with multiphase systems, such as the front-tracking method, volume-of-fluid (VOF) method, level set method; and approaches based on minimum-surface-energy can only describe static surface morphology and are not able to give dynamic information on the velocity field.

In the past two decades, the Lattice Boltzmann method (LBM), which is a mesoscopic approach based on minimal lattice formulations of the kinetic Boltzmann equation, has been developed into an efficient tool to model interfacial phenomena in multiphase and multicomponent flows (Huang et al., 2015). Moreover, the LBM has also shown its ability to handle self-propelled motion problems. Chen et al. (2011) simulated interfacial Marangoni convection in gas-liquid mass transfer by LBM. Fu et al. (2016) studied the double emulsion formation in microchannels by a ternary Lattice Boltzmann method. A two-dimensional mass conserving LBM was developed by Joshi and Sun (2009) for multiphase flows with solid particles suspended within the liquid or vapor phases. Lattice Boltzmann simulation of particle motion in binary immiscible fluids was carried out by Chen et al. (2015). The self-propelled motion of Leidenfrost droplets on ratchet-shaped surfaces is numerically investigated by Li et al. (2016) with a thermal multiphase LBM model. In addition, integrating the Lattice Boltzmann and immersed boundary methods, Shum et al. (2013) established a model to study self-propelled particles with active, reconfigurable surfaces.

Among multiphase LBMs available in the literature, the pseudopotential multiphase model is the most widely used because of its remarkable computational simplicity. This model was originally proposed by Shan and Chen (Shan and Chen, 1993, 1994), and its intermolecular interactions are represented by a density-dependent pseudopotential. In this paper, we use the Shan and Chen pseudopotential model to explore the meniscus-induced motion of droplets and bubbles. However, the meniscus-induced motion problem usually involves at least three fluid phases (air, water and droplet/bubble) and to the best of the authors' knowledge, there are few studies reported on three-phase LBM models and their application (other than models where the third phase is the solid phase). Therefore, a three-phase pseudopotential model is validated first and it is shown that the model is capable of simulating the three-phase separation process as well as the meniscus-induced motion of a bubble. Subsequently, we simulate an air/water meniscus using the model and place a droplet/bubble of a third component (e.g., oil) on the meniscus. By observing the motion of the droplet/bubble, we discuss how the surface tension, gravity, droplet/bubble size, and meniscus curvature influence the spontaneous motion.

2. Model and theory

In this section, the Lattice Boltzmann method and pseudopotential multiphase model are introduced briefly, as well as the three phase, three component LBM pseudopotential model.

2.1. Lattice Boltzmann method

The Lattice Boltzmann equation, which governs the evolution of the density distribution, can be derived from the BGK approximation of the Boltzmann equation, and is expressed as follows (Bhatnagar et al., 1954):

$$f_i(\mathbf{x}+\mathbf{e}_i\Delta t, t+\Delta t) = f_i(\mathbf{x},t) - \frac{1}{\tau}(f_i(\mathbf{x},t) - f_i^{eq}(\mathbf{x},t)) + S_i(\mathbf{x},t), \quad (1)$$

where $f_i^{eq}(\mathbf{x},t)$ is the density distribution function, $\mathbf{x}$ is the spatial position, $\mathbf{e}_i$ is the discrete velocity along the ith lattice direction, τ is the relaxation time, $S_i(\mathbf{x},t)$ represents the forcing term in the velocity space, and $f_i^{eq}(\mathbf{x},t)$ is the corresponding equilibrium distribution function.

The discrete velocities and equilibrium distribution functions depend on the particular velocity model. For a D2Q9 (two-dimensional, nine velocity) model, the discrete velocities are defined as:

$$\mathbf{e}_i = \begin{cases} (0,0) & i=0 \\ c(\cos[i-1]\frac{\pi}{2}), \sin\left[(i-1)\frac{\pi}{2}\right] & i=1-4 \\ \sqrt{2}c(\cos\left[(2i-1)\frac{\pi}{4}\right], \sin\left[(2i-1)\frac{\pi}{4}\right]) & i=5-8 \end{cases}, \quad (2)$$

where $c = \Delta x/\Delta t$ is the lattice speed with Δx and Δt the lattice spacing and time step (both Δx and Δt equal 1 in the lattice system of units).

The equilibrium distribution function for the D2Q9 lattice is:

$$f_i^{eq}(\mathbf{x},t) = \omega_i\rho\left[1 + \frac{\mathbf{e}_i\cdot\mathbf{u}}{c_s^2} + \frac{(\mathbf{e}_i\cdot\mathbf{u})^2}{2c_s^4} - \frac{\mathbf{u}^2}{2c_s^2}\right], \quad (3)$$

where the weight factors w_i are given by $w_0 = 0, w_{1-4} = 1/9, w_{5-8} = 1/36$, and c_s is the sound speed. ρ and $\mathbf{u}$ are the macroscopic density and the macroscopic velocity vector respectively, which can be calculated from:

$$\rho = \sum_i f_i, \quad (4)$$

$$\mathbf{u} = \frac{1}{\rho}\sum_i f_i\mathbf{e}_i. \quad (5)$$

In addition, it is well known that the Navier-Stokes equations can be recovered from the Lattice Boltzmann equation using Chapman-Enskog expansion (Qian et al., 1992).

2.2. Three-phase pseudopotential Lattice Boltzmann model

The pseudopotential multiphase model includes two subtypes, namely the single component multiphase (SCMP) model and the multicomponent multiphase (MCMP) model (Sukop and Thorne, 2006). In the SCMP model, a long-range attractive force is added between 'particles' in the LBM model to enable phase separation into a liquid and its own vapor following a van der Waals-like Equation of State (EOS).

In the MCMP model (2 'chemical' components corresponding to 2 fluid phases in most cases), a long range repulsive force between different components is added so that a hydrophobic type of phase separation of different chemical components can be realized. The interaction force acting on σ th component is defined as Shan and Chen (1993):

$$\mathbf{F}_{\text{int},\sigma}(\mathbf{x},t) = -G_{\text{int}}\psi_\sigma(\mathbf{x},t)\sum_i \omega_i\psi_{\overline{\sigma}}(\mathbf{x}+\mathbf{e}_i\Delta t, t)\mathbf{e}_i, \quad (6)$$

where $\psi_\sigma(\rho_\sigma)$ is an effective mass depending on the local density, the σ and $\overline{\sigma}$ represent two different components. $\psi_\sigma(\rho_\sigma)$ is commonly taken as the density, $\psi_\sigma = \rho_\sigma$. And G_{int} is a parameter that controls the interaction force, and hence controls the interfacial tension.

In the literature, at least five studies that simulated three immiscible components (Semprebon et al., 2016; Fu et al., 2016; Bao and Schaefer, 2013; Leclaire et al., 2013; Van Kats and Egberts, 1999) using LBM model. The color-gradient LBM model are used the most among these studies, and few show the applications of the pseudopotential LBM model. That's because the SCMP and MCMP pseudopotential models both suffer from some problems in simulating a third phase. For some of the possible models, a single phase can actually be a mixture of multiple components, and unfortunately, the properties of the mixture phase are not obvious and therefore such a three-phase system is not optimal for studying the meniscus-induced motion of droplets. In contrast, for the MCMP model when only interaction forces between different components are considered and with one additional component C_3 added to the original system composed of components C_1 and C_2, a pure three phase system appears (3C3P). As there is no force between like particles of any one component considered, the density ratio between different components is relatively low and thus may not be able to adequately represent meniscus-induced motion problems in liquid-gas systems. But the surface tension in MCMP model can be tuned independently of the density ratio by changing the strength of the interaction force G_c, which is rather difficult in the SCMP model (Li and Luo, 2013). Thus if the density ratio effect in the meniscus-induced motion problems can be incorporated or treated properly, the MCMP scheme would be a better choice to study the meniscus-induced motion of droplets. One possible approach could be to use an effective density as in Ngachin et al. (2015) and Ren et al. (2016).

In this paper, the three component/three phase MCMP model is used (each phase include only one component). The interaction force on the σ_k th component is:

$$\mathbf{F}_{\text{int},\sigma_k}(\mathbf{x},t) = -\rho_{\sigma_k}(\mathbf{x},t)\sum_{j\neq k} G_{\text{int},\sigma_k\sigma_j}\sum_i \omega_i\rho_{\sigma_j}(\mathbf{x}+\mathbf{e}_i\Delta t, t)\mathbf{e}_i \quad (7)$$

where σ_k and σ_j represent different components and $G_{\text{int},\sigma_k\sigma_j}$ is a parameter that controls the interaction force between these two components.

The solid surface force on the σ th component can be computed as follows (Martys and Chen, 1996)

$$\mathbf{F}_{\text{ads},\sigma}(\mathbf{x},t) = -G_{\text{ads},\sigma}\rho_\sigma(\mathbf{x},t)\sum_i \omega_i s(\mathbf{x}+\mathbf{e}_i\Delta t, t)\mathbf{e}_i, \quad (8)$$

where the $s(\mathbf{x}+\mathbf{e}_i\Delta t, t)$ is an indicator function that is equal to 1 or 0 for a solid or fluid domain node, $G_{\text{ads},\sigma}$ is a parameter that controls the strength of the interfacial tension between the solid and σ th component.

In the MCMP model, the macroscopic velocity $\mathbf{u}^{eq}$ is used instead of $\mathbf{u}$ when calculating the equilibrium distribution function with Eq. (3). The $\mathbf{u}^{eq}$ of the σ th component is given by

$$\mathbf{u}^{eq} = \mathbf{u}\prime + \frac{\tau_\sigma(F_{\text{int},\sigma} + F_{\text{ads},\sigma} + F_{\text{b},\sigma})}{\rho_\sigma}, \quad (9)$$

where $F_{\text{b},\sigma}$ is the external force or body force, and $\mathbf{u}\prime$ is a composite macroscopic velocity defined as

$$\mathbf{u}\prime = \frac{\sum_\sigma\left(\sum_i \frac{f_i^\sigma\mathbf{e}_i}{\tau_\sigma}\right)}{\left(\sum_i \frac{\rho_i^\sigma}{\tau_\sigma}\right)}. \quad (10)$$

The pressure in the three phase MCMP model is

$$p = c_s^2\sum_i \rho_{\sigma_i} + c_s^2\sum_i\sum_{j\neq i} G_{\text{int},\sigma_i\sigma_j}\rho_{\sigma_i}\rho_{\sigma_j}. \quad (11)$$

The model can also be improved by using more accurate forcing schemes and corresponding velocity, and pressure equations. The more details can be found in Guo and Shu (2013), Sega et al. (2013), and Sbragaglia and Belardinelli (2013).

3. Model verification

In this section, the phase separation phenomenon was simulated to test the three phase LBM model; this is the most basic example in two phase LBM-related literature. The numerical results were qualitatively compared with the data from the mathematical topology literature that constitute appropriate tests of the three phase configurations. Then an effective density technique is developed to incorporate the large density ratio effect in a gas-liquid system and the meniscus-induced motion of a bubble is simulated. Finally, we compared velocity profiles of the LBM simulations in the layered three-phase flow with the analytical solution and find that the relative error is around 2%.

3.1. Three phase separation

The three components C_1, C_2, C_3 are initialized with a density of 0.3 ± 0.001 randomly in a 200 lu × 200 lu (lu is the length unit and is equal to one lattice spacing in our LBM models) domain as an initial state before phase separation. Periodic boundary conditions are applied on all the boundaries and the relaxation time parameters of three components are all set to 1.0. Denote $G_{\text{int},ij}$ as the parameters that control the strength of the interaction forces (interfacial tension) between C_i and C_j. Then different interaction force parameters will lead to different phase separation patterns and each phase will include only one component ignoring with small dissolved amounts of the other components (Sukop and Thorne, 2006). Fig. 1 shows four separation simulation results using different interaction force parameters at $t = 20{,}000$ time steps (i.e., 20,000 ts, where ts is the time unit in our LBM models), from which we can summarize the typical phase morphologies that may appear during the separation: polygonal shape, circular or elliptical shape, disconnected pieces shape and connected pieces shape (these patterns are listed in Fig. 1). Similar patterns can also be found in Semprebon et al. (2016). The polygonal shape of one phase would be more regular if the interaction force between the other two components decreases (C_1 in Fig. 1(a) to C1 in Fig. 1 (b), $G_{\text{int},23}$ decreases), and the polygonal shape can even turn to circular or elliptical shape in another simulation when this force decreases further. The disconnected pieces shape of one phase appears if the interaction force between the other two components is dominant (C_1 in Fig. 1(c), $G_{\text{int},23}$ is 1.5 times the strength of others), and when this dominant interaction force is large enough, the pieces would be connected (C_1 in Fig. 1(d), $G_{\text{int},23}$ is 2.3 times the strength of others).

Moreover, we find that the polygonal structure during the separation of the three phases similar to the structure of foam films, which follow Plateau's laws (Taylor, 1976). Fig. 2 shows a structure of foam films created with soapy water. In comparing it with Fig. 1 (a) and 1(b), we find the following common points: (1) three and only three films/phases meet at a vertex, which is a result of principle of minimum energy; (2) the average number of sides is 6, which is a requirement of the Euler characteristic. There are also some differences in that the number of edges per bubble in a foam can be an odd number while in phase separation structures it has to be even. This can be proved by reduction to absurdity. Given that phases meet at a vertex must be different with each other in a three phase system, and if we fill another two different colors on edges of a polygon with odd edge number, we could never make it for there are always two adjacent edge having the same color. Besides, the polygonal shapes in phase separation structures can be curved-sided polygons.

In addition, the model also provides an alternative way to solve the double bubble problem, which is a generalization of the isoperimetric problem. Corneli et al., 2004 studied the double

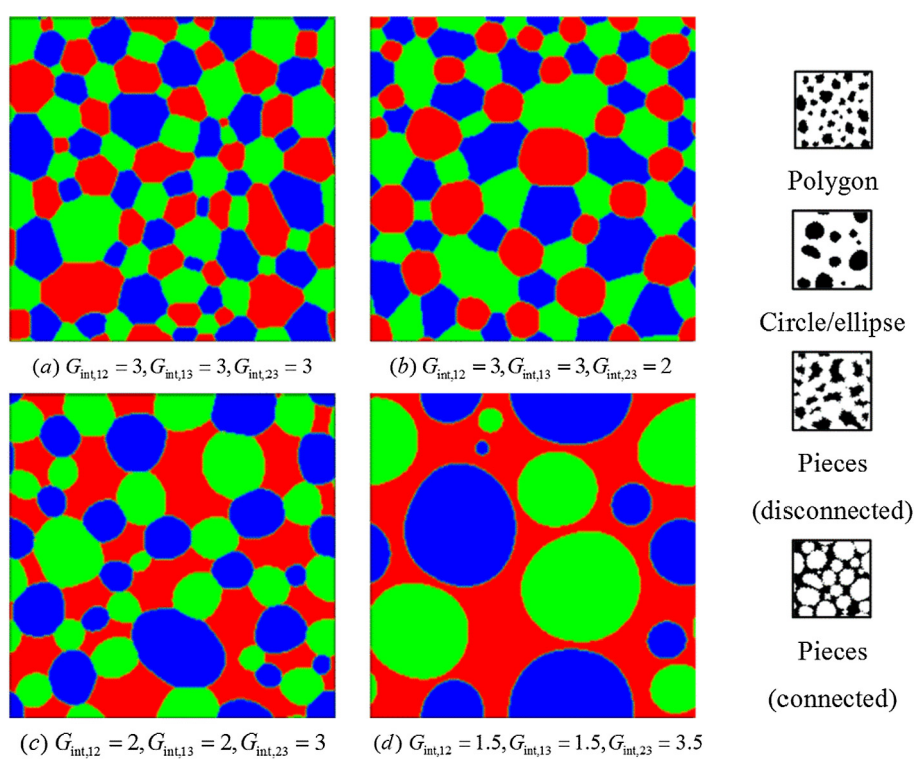

Fig. 1. Typical phase morphologies and LBM simulations of three phase separation with different interaction forces. The morphology patterns are indicated with black color. The red, green, and blue colors represent C_1, C_2, and C_3 respectively. (For interpretation of the references to colour in this figure legend, the reader is referred to the web version of this article.)

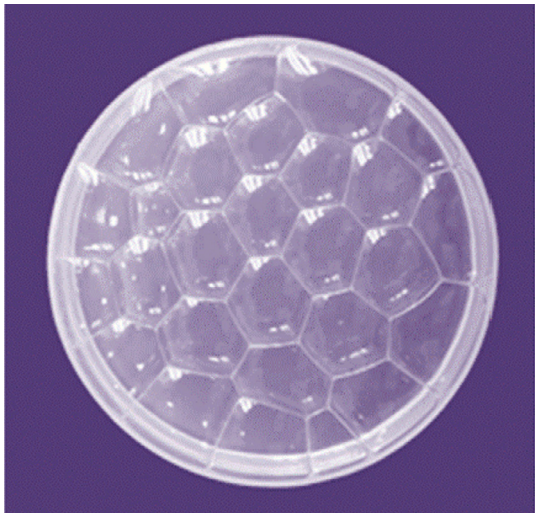

Fig. 2. Foam films created with soapy water in a petri dish, taken by phone camera in the lamplight at room temperature.

bubble problem on the flat two-torus and showed that there are some types of the double bubble topology on different tori. Setting different initial conditions in a periodic domain (corresponding to the flat torus) leads to different volumes of the three components. LBM simulation can obtain the same topological structures, i.e., the standard double bubble, a standard chain, the band lens, the double band, as the found in the literature (Gillard and Sutcliffe, 2009) and shown in Fig. 3.

3.2. Meniscus-induced motion of a bubble

It is well known that bubbles near a meniscus tend to migrate to the wall. Fig. 4 shows the phenomenon in which a bubble floats on the water surface and migrates to the wall induced by the meniscus in a glass-walled cup. The experiment is performed in normal room temperature, roughly 25 °C. The contact angle between the meniscus and the wall is 70°, and the bubble's radius is about 1.0 cm. Soapy water was mixed in a syringe and used to place a stable bubble on the water surface in the cup. The surface tension of water is 72×10^{-3} N/m and that of soapy water is approximately 25×10^{-3} N/m. So the interfacial tension of the bubble in the air is 50×10^{-3} N/m in consideration of its double liquid-vapor interfaces.

The above bubble motion was also simulated by the MCMP LBM. In the simulation, C_1, C_2, C_3 represent water, air, and bubble, respectively. Dimensionless parameters can be used to connect the real system with the simulated system by similarity principles, and then the simulation can reflect the features of the real system. In the above two systems, the interfacial tension ratio, the density ratio, and the dimensionless pseudo-Bond number, which we define below for our particular three phase case, must be consistent. The pseudo-Bond number is defined as

$$Bop = \frac{\rho_3 g r^2}{\gamma_{12}}, \tag{12}$$

where ρ_3 is the density of C_3, g is the gravitational acceleration, γ_{12} is the interfacial tension between C_1 and C_2, and r is the radius of C_3.

The initial state of the simulation is shown in Fig. 5. The three phases are distributed in a $200 \times 100\ \mathrm{lu}^2$ tank whose boundaries

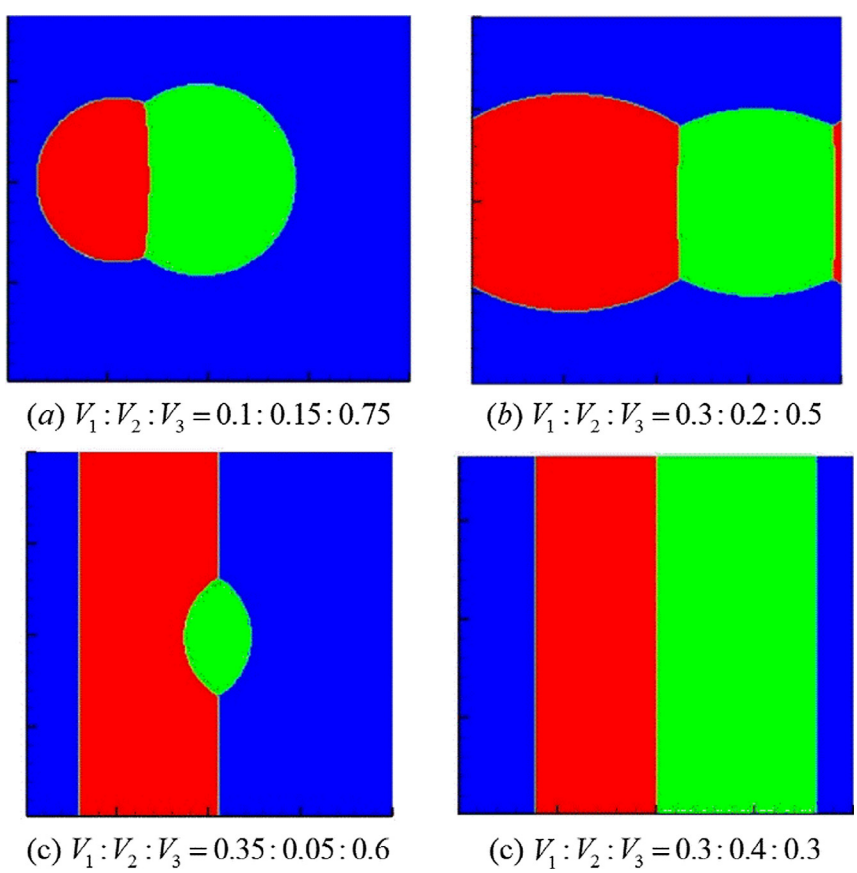

Fig. 3. LBM simulations of double bubble problem, the V_1, V_2, and V_3 represent the volume of C1, C2, and C3 respectively.

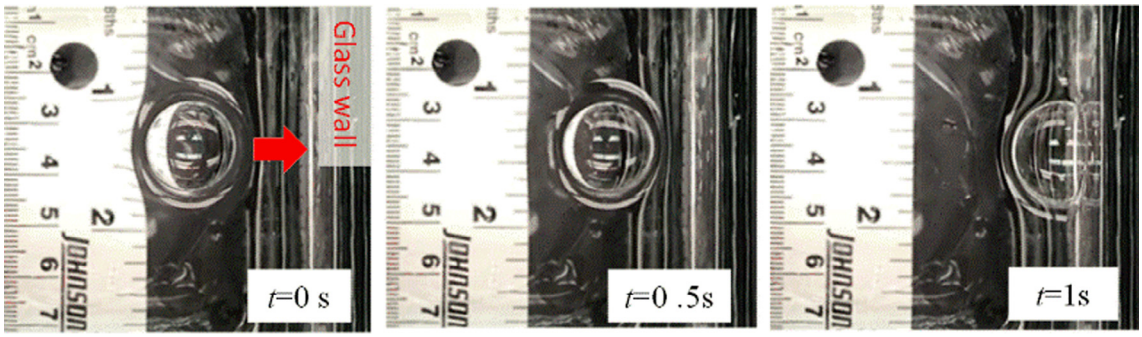

Fig. 4. Meniscus-induced motion of a bubble, top view, recorded by phone camera.

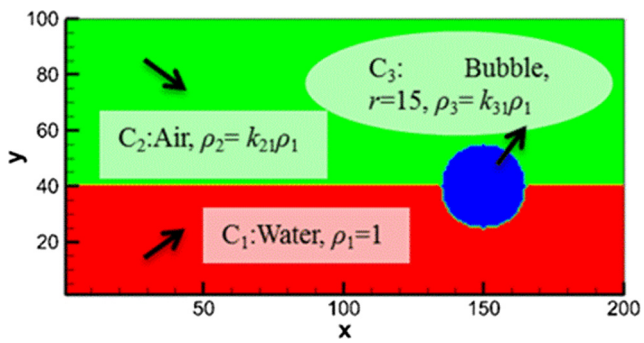

Fig. 5. Initial state of the LBM simulation of the bubble motion.

are all solid; the upper portion of the tank is filled with air, the lower portion is full of water, and a bubble whose radius is 15 lu is placed on the water surface at $x = 150$, $y = 40$. For convenience, each node only contains one component and the density of every node except the solid boundaries is set to 1.0 in the initial condition. First and foremost, we select the interaction parameters G_{int} to make sure that $\gamma_{12} : \gamma_{13} : \gamma_{23} = 72 : 72 : 50$. As the density of each component is 1.0, it is straightforward to select G_{int} according to the relationship between scaled component densities and scaled lattice surface tension, which has been summarized by Huang et al. (2007). Here we choose $G_{\text{int},12} = 3, G_{\text{int},13} = 3, G_{\text{int},23} = 20.25$, and in this case the interfacial tension $\gamma_{12} = 0.1794 \quad \text{lu} \cdot \text{mu} \cdot \text{ts}^{-2}$. Then we calculate the pseudo-Bond number and select the gravitational acceleration in the simulation. In this experiment, the pseudo-Bond number based on the real density of the air phase, Earth's gravitational acceleration, a 0.01 m radius bubble, and the standard air/water interfacial tension is

$$Bop = \frac{\rho_3 g r^2}{\gamma_{12}} = \frac{1.29\text{kg/m}^3 \times 10\text{m/s}^2 \times (1 \times 10^{-2}\text{m})^2}{72 \times 10^{-3} N/\text{m}} = 0.018, \tag{13}$$

Subsequently, the gravitational acceleration in the simulation can be determined by the similarity principle requiring equal pseudo-Bond numbers:

$$g_{LBM} = \frac{Bop \cdot \gamma_{12}}{\rho_3 r^2} = \frac{0.018 \times 0.1794}{1 \times 15^2} = 1.5 \times 10^{-5} \text{ lu/ts}^2. \tag{14}$$

Finally, we have to deal with the large density ratio between the air and liquid phases. We account the low density of the air phase using an effective density approach as Ngachin et al. (2015) and Ren et al. (2016). Thus the density ratio is only accounted for by different gravity applied to different phases in this three phase system. In reality, other fluid properties vary with the density. Because these simulations represent quasi-static conditions, the assumption is appropriate. Then if we use the body force with the adjusted values of the gravity instead, the large density ratio can be appropriately incorporated. In such a quasi-static condition, we mainly focus on the role of surface tension and gravity. Though the viscosity only depends on the relaxation time ($\nu = c_s^2(\tau - 0.5)$) in LBM model and can vary independent of density, we suggest use the same relaxation time for all three components so that we can control the surface tension easily and get a better numerical stability during simulation. Denote $k_{\sigma\bar{\sigma}}$ as the density ratio between component σ and $\bar{\sigma}$, then $k_{31} = \rho_3/\rho_1 = \rho_{\text{air}}/\rho_{\text{water}} \approx 0.001$, $k_{21} = \rho_2/\rho_1 \approx 0.001$, and the body forces for C_1, C_2, and C_3 are given by $F_{\text{b},1} = \rho_1 g_{LBM}$, $F_{\text{b},2} = k_{21}\rho_1 g_{LBM}$, $F_{\text{b},3} = k_{31}\rho_1 g_{LBM}$, respectively.

Bounce-back boundary conditions are applied on the four boundaries and the key parameters in the simulation system are listed in Table 1. In addition, G_{ads} can be adjusted to control the contact angle between different components, which we discuss in the next section. The simulation results are shown in Fig. 6. The bubble uses about $t = \sqrt{\frac{g_{LBM}}{g}\frac{\Delta L}{\Delta L_{LBM}}}ts = \sqrt{\frac{1.5\times10^{-5}}{10}\frac{0.03}{50}} \times 3\times 10^4 = 0.9$ s to arrive at the wall, where ΔL and ΔL_{LBM} means the distance between the wall and the bubble in experiment and LBM simulation and can be measured from Fig. 4 and Fig. 5, respectively. The results show that the three phase model can simulate the spontaneous motion successfully and the simulation results can give detailed information of the physical process at different time steps, such as the meniscus shape, the bubble shape, the bubble position (thus the velocity), and so on.

3.3. Layered three-phase flow

Here we consider immiscible layered three-phase flow in a 2D channel, as described in Fig. 7. Phase 1 flows in the central region $0 < |y| < a$, phase 2 flows in the region $a < |y| < b$, and phase 3 flows in the region $b < |y| < c$. According to N-S equations, the flow of each phase governed by:

$$\begin{cases} \rho_1 \nu_1 \nabla^2 u_1 = -F_{\text{b},1} \\ \rho_2 \nu_2 \nabla^2 u_2 = -F_{\text{b},2}, \\ \rho_3 \nu_3 \nabla^2 u_3 = -F_{\text{b},3} \end{cases} \tag{15}$$

Table 1
Parameters (lattice unit) for LBM simulation of the bubble motion.

Parameters	Value
τ_1, τ_2, τ_3	1, 1, 1
$G_{\text{int},12}$, $G_{\text{int},13}$, $G_{\text{int},23}$	3, 3, 2.25
$G_{\text{ads},1}$, $G_{\text{ads},2}$, $G_{\text{ads},3}$	−0.15, 0.2, 0.1
g_{LBM}	0.000015
k_{31}, k_{32}	0.001, 0.001

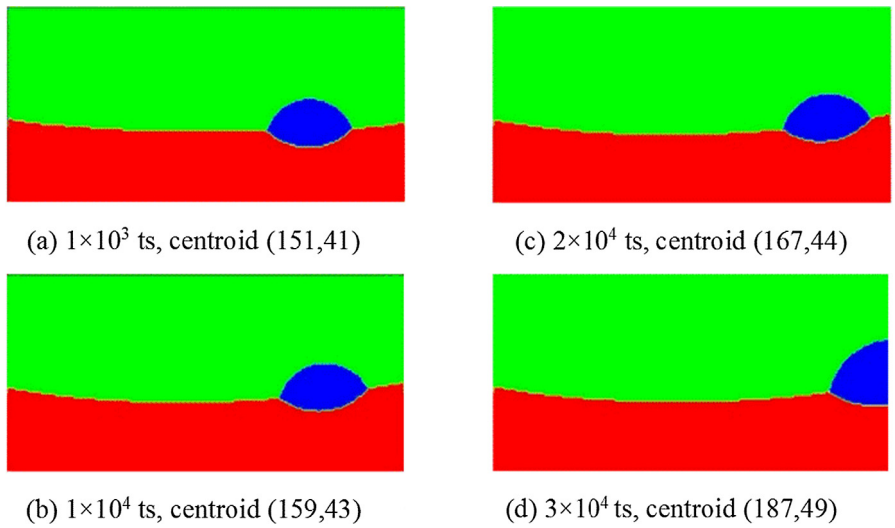

Fig. 6. LBM simulation of meniscus-induced bubble motion at different time steps, the red, green, and blue colors represent water, air, and bubble respectively. (For interpretation of the references to colour in this figure legend, the reader is referred to the web version of this article.)

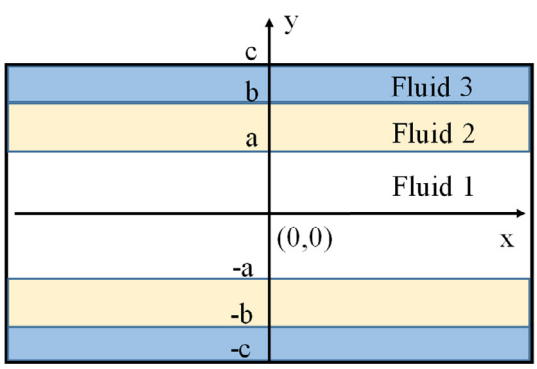

Fig. 7. Immiscible three-phase flow in a 2D channel.

where ν_i is the kinematic viscosity, u_i is the velocity of each phase.

The boundary conditions are:

$$\begin{cases} \frac{\partial u_1}{\partial y}|_{y=0}=0, \quad \rho_1\nu_1\frac{\partial u_1}{\partial y}|_{y=a}=\rho_2\nu_2\frac{\partial u_2}{\partial y}|_{y=a}, \quad \rho_2\nu_2\frac{\partial u_2}{\partial y}|_{y=b}=\rho_3\nu_3\frac{\partial u_3}{\partial y}|_{y=b} \\ u_1|_{y=a}=u_2|_{y=a}, \quad u_2|_{y=b}=u_3|_{y=b}, \quad u_3|_{y=c}=0 \end{cases}. \tag{16}$$

Assuming Poiseuille-type flow in the channel, the analytical solution for the velocity profile plates can be obtained:

$$u_i = A_i y^2 + B_i y + C_i, \; i = 1,2,3 \tag{17}$$

$$A_1 = -\frac{F_{b,1}}{2\rho_1\nu_1}, \quad A_2 = -\frac{F_{b,2}}{2\rho_2\nu_2}, \quad A_3 = -\frac{F_{b,3}}{2\rho_3\nu_3},$$

$$B_1 = 0, \quad B_2 = M_{12}A_1 a - 2A_2 a, \quad B_3 = 2M_{23}A_2 b - 2A_3 b + M_{23}B_2, \quad M_{ij} = \rho_i\nu_j/\rho_i\nu_{ij}$$

$$C_1 = (A_2 - A_1)a^2 + B_2 a + C_2, \quad C_2 = (A_3 - A_2)b^2 + (B_3 - B_2)b + C_3, \quad C_3 = -A_3c^2 - B_3c.$$

By setting $a = 20$, $b = 35$, $c = 50$, $M_{12} = M_{23} = 1$ and $F_{b,1} = 0$, $F_{b,2} = 2.5 \times 10^{-5}$,$F_{b,3} = 5 \times 10^{-5}$, the relaxation time and density of three components being set to 1.0, and interaction parameters being set to 2.0, layered three-phase flow is simulated using the model in a 10×101 domain. The top and bottom are solid and the boundaries along the x direction are periodic. The velocity profiles at $x = 5$ are compared with the analytical solution, as shown in Fig. 8. The numerical results are good and the relative error is less than 2%. But there are small jumps across the interfaces, especially the interface between phase 2 and phase 3.

To summarize, the model is capable of simulating both basic phase separation and the practical problem of the meniscus-induced motion of a bubble. It is also consistent with topologic requirements. The agreement between the experiment result, analytical solution and the LBM simulations validated our MCMP LBM code. We believe this model also works in three dimensions, but a three-dimension velocity model should be used. In the next section, we will explore the meniscus-induced motion of droplets and bubbles in-depth using the model.

4. Results and discussion

In this section, how the interfacial tension (droplet shape), gravity, droplet/bubble size, and the curvature of the meniscus influence the self-propelled droplet/bubble motion are discussed.

4.1. Influence of the droplet shape on the motion

4.1.1. Droplet shape on the interface

We begin with a droplet of radius 15 lu placed on the horizontal interface between the other two components in a domain size of

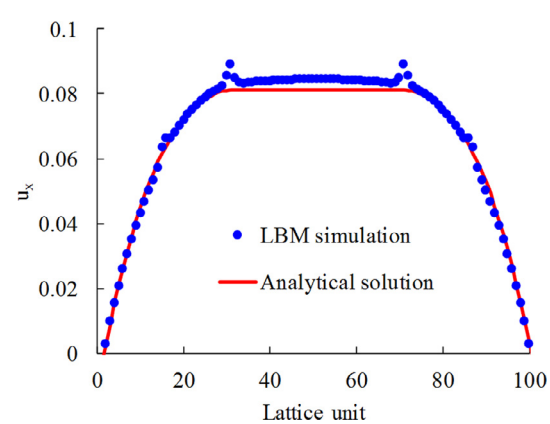

Fig. 8. Comparison of velocity profiles from LBM simulation and analytical solution.

$100 \times 100\,\mathrm{lu}^2$ as shown in Fig. 9. The top and bottom are solid walls where bounce-back boundary conditions are applied, while the left and right boundaries are periodic. As in the previous simulations, the relaxation times and the initial densities are all set to 1.0.

$G_{\mathrm{int},12}$, $G_{\mathrm{int},13}$, and $G_{\mathrm{int},23}$ can represent the effects of γ_{12}, γ_{13}, and γ_{23} because the interaction force parameters are basically proportional to the interfacial tensions (Huang et al., 2007). So, different interaction force parameters lead to different interfacial tensions and the droplet will evolve gradually into different shapes depending on the value of G_{int} . The force analysis schematic of this system is presented in Fig. 10 to help understanding the basic rules of the shape evolution. In order to design a particular droplet shape with different interaction force parameters, the following equations are analyzed based on the force balance model:

$$\begin{cases} \gamma_{12} = \gamma_{23}\cos\theta_2 + \gamma_{13}\cos\theta_1 \\ \gamma_{23}\sin\theta_2 = \gamma_{13}\sin\theta_1 \end{cases} \tag{18}$$

With interfacial tensions known, θ_1 and θ_2 can be expressed as functions of γ_{12}, γ_{13}, and γ_{23} . Unfortunately, it is hard to solve Eq. (18) directly because the trigonometric functions are involved. Here we provide a simple approach by solving triangles. In ΔABD shown in Fig. 11, apply the cosine law on $\angle BAD$,

$$\cos(180^\circ - (\theta_1+\theta_2)) = -\cos(\theta_1+\theta_2) = \frac{\gamma_{13}^2+\gamma_{23}^2-\gamma_{12}^2}{2\gamma_{13}\gamma_{23}}, \tag{19}$$

then the law of sines on ΔABD gives,

$$\frac{\sin\theta_1}{\gamma_{23}} = \frac{\sin\theta_2}{\gamma_{13}} = \frac{\sin(180^\circ - (\theta_1+\theta_2))}{\gamma_{12}} = \frac{\sin(\theta_1+\theta_2)}{\gamma_{12}}. \tag{20}$$

By considering Eq. (19) and Eq. (20) simultaneously, we obtain

$$\frac{\sin\theta_1}{\gamma_{23}} = \frac{\sin\theta_2}{\gamma_{13}} = \frac{\sqrt{1-\left(\frac{\gamma_{12}^2-(\gamma_{13}^2+\gamma_{23}^2)}{2\gamma_{13}\gamma_{23}}\right)^2}}{\gamma_{12}}. \tag{21}$$

Thus we can predict the droplet shape when the interfacial tensions are known. For example, we may be concerned about the degree of flatness of the droplet, and we can use the equation $\cos(\theta_1+\theta_2) = \frac{\gamma_{12}^2-(\gamma_{13}^2+\gamma_{23}^2)}{2\gamma_{13}\gamma_{23}}$ to calculate $\theta_1+\theta_2$ in advance. In LBM models, the proportional relationship between component interaction parameters and interfacial tensions is very close to linear. Therefore, we can use the component interaction parameters instead of interfacial tensions in Eq. (21) so that we can conveniently design different droplet shapes:

$$\frac{\sin\theta_1}{G_{\mathrm{int},23}} = \frac{\sin\theta_2}{G_{\mathrm{int},13}} = \frac{\sqrt{1-\left(\frac{G_{\mathrm{int},12}^2-\left(G_{\mathrm{int},13}^2+G_{\mathrm{int},23}^2\right)}{2G_{\mathrm{int},13}G_{\mathrm{int},23}}\right)^2}}{G_{\mathrm{int},12}}. \tag{22}$$

To test the accuracy of this estimation method, eight simulation results with different component interaction parameters are shown in Fig. 12. Gravity is ignored in these simulations. We measured the contact angles using Huang's method (2007) and compare them with the expectations calculated using Eq. (22). The comparison results are listed in Table 2. Cases (c) and (g) are not listed because they are symmetrical with cases (b) and (f). The comparison shows that the contact angles calculated with Eq. (22) agree well with the measured ones over most of the range. It also shows the basic evolution rules that γ_{12} controls the degree of flatness of droplet shape on the whole, while γ_{13} and γ_{23} determine the degree of symmetry of the droplet shape. To be specific, the bigger γ_{12} is, the flatter the droplet shape, because γ_{12} pulls

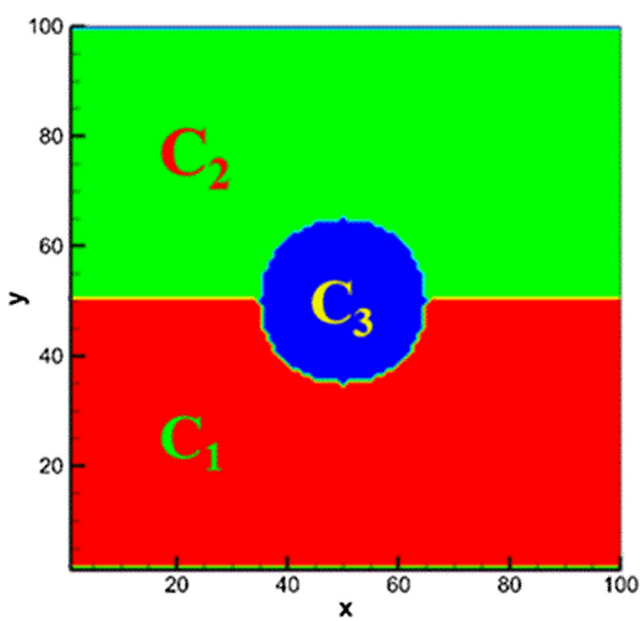

Fig. 9. Initial state of the bubble simulation. The red, green, and blue colors represent C_1, C_2, and C_3 respectively. (For interpretation of the references to colour in this figure legend, the reader is referred to the web version of this article.)

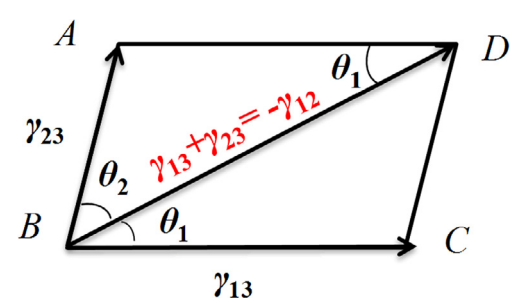

Fig. 11. Schematic for solving triangles.

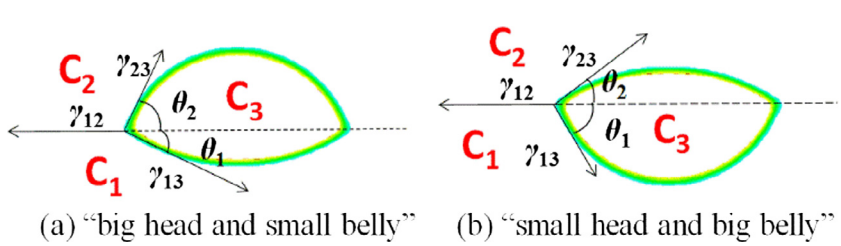

Fig. 10. Force analysis schematic for a droplet between two other components.

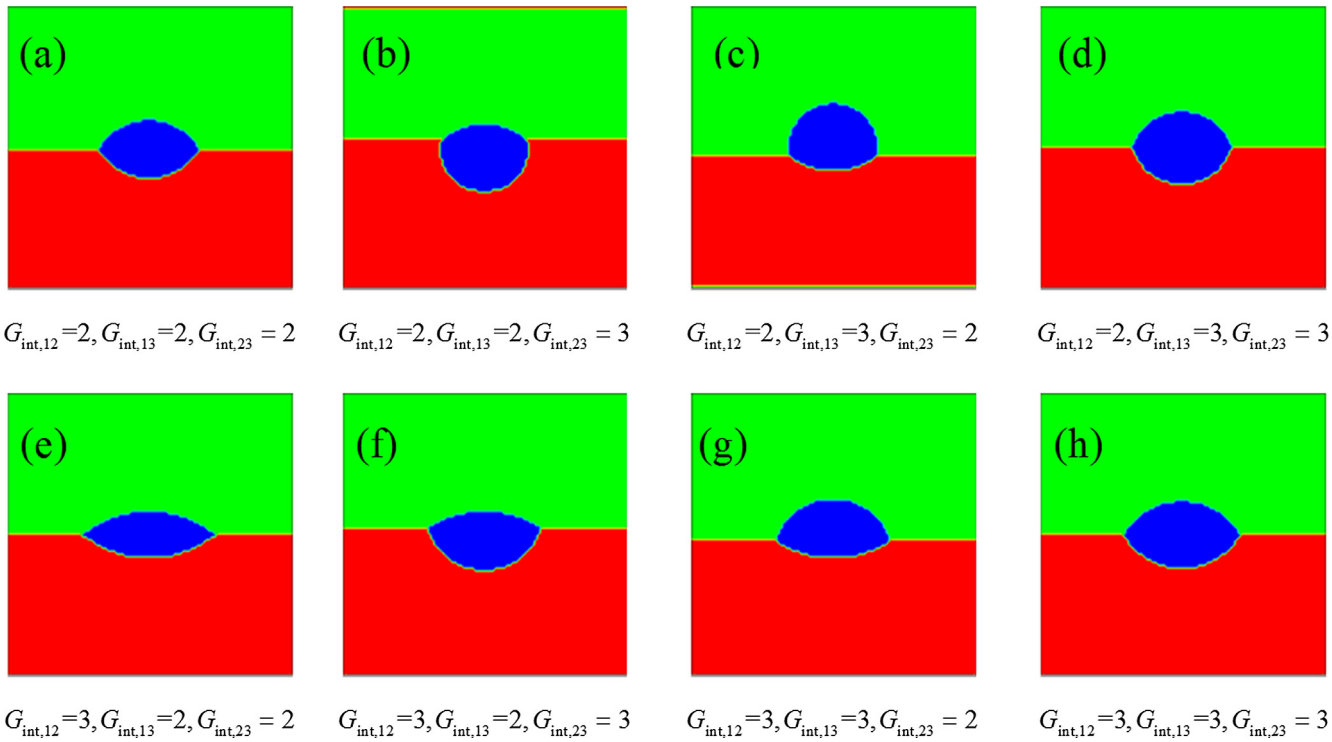

Fig. 12. LBM simulations of droplets shape with different interaction force parameters.

the droplet outward from both sides. Meanwhile, the bigger γ_{23} is, the smaller θ_2 becomes, and the same holds for γ_{13} and θ_1 . In addition, the shape is symmetrical if γ_{23} is equal to γ_{13}.

Table 2
Measured and estimated contact angles (degrees) for a droplet.

Case	θ_1		θ_2	
	Fig. 9	Eq. (22)	Fig. 9	Eq. (22)
a	61.25	60.00	61.52	60.00
b	97.31	97.18	43.97	41.41
d	73.04	70.53	73.14	70.53
e	41.46	41.40	41.09	41.40
f	72.89	70.53	37.80	38.94
h	61.29	60.00	61.54	60.00

4.1.2. Motional tendency of droplets with different shapes

Ignoring gravity, droplets with different shapes on a concave or convex meniscus are simulated to study their movement trends governed by geometrical gradients. Droplets move due to the curvature and curvature gradient of the menisci. Simulations are carried out in a $200 \times 100\,\mathrm{lu}^2$ tank and the results show that the droplet tends to move to the wall on a concave upward meniscus when $\theta_2/\theta_1 > 1$, whereas it tends to move to the center of the meniscus when $\theta_2/\theta_1 \leqslant 1$. Moreover, droplets present a contrary tendency when the meniscus is convex; because there is no gravity in the simulations, the convex case is simply the vertical inversion of the simulations in Tables 3 and 4. Table 3 gives information about the motion of a droplet when θ_2 is greater than θ_1 . The droplet centroid is at (130, 40) initially and the parameters are set to

Table 3
Motion of asymmetrical droplets on concave meniscus when $\theta_2 > \theta_1$. The left, middle, and right columns represent different cases. All droplets eventually reach the wall.

Time	$G_{int,12}$=3, $G_{int,13}$=2.6, $G_{int,23}$ = 2	$G_{int,12}$=3, $G_{int,13}$=3, $G_{int,23}$ = 2	$G_{int,12}$=3, $G_{int,13}$=3.4, $G_{int,23}$ = 2
1×10^4 ts	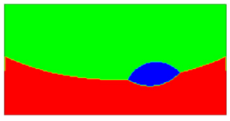	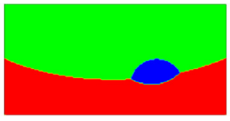	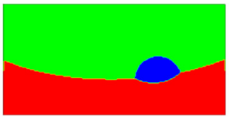
	(a) centroid (134,37)	(a') centroid (135,39)	(a'') centroid (138,41)
3×10^4 ts	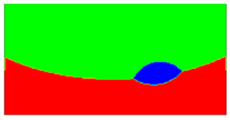	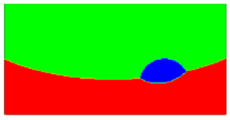	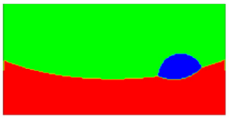
	(b) centroid (138,38)	(b') centroid (142,39)	(b'') centroid (158,43)
5×10^4 ts	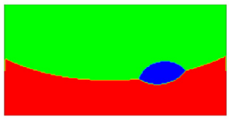	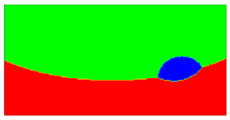	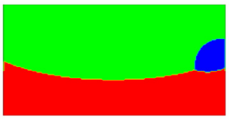
	(c) centroid (141,38)	(c') centroid (157,42)	(c'') centroid (187,53)

Table 4
Motion of asymmetrical droplets on concave meniscus when $\theta_2 < \theta_1$. The left, middle, and right columns represent different cases.

Time	$G_{int,12}=3, G_{int,13}=1.6, G_{int,23}=3$	$G_{int,12}=3, G_{int,13}=2, G_{int,23}=3$	$G_{int,12}=3, G_{int,13}=2.2, G_{int,23}=3$
1×10^4 ts	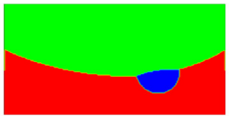	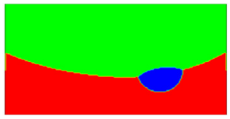	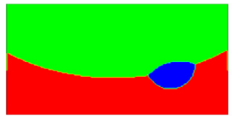
	(a) centroid (140,31)	(a') centroid (141,33)	(a'') centroid (150,36)
5×10^4 ts	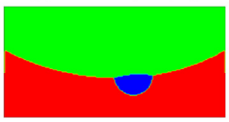	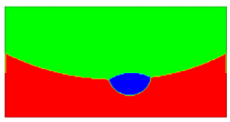	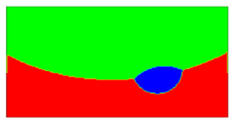
	(b) centroid (117,30)	(b') centroid (113,31)	(b'') centroid (138,34)
12×10^4 ts	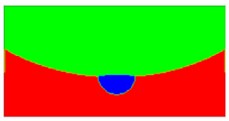	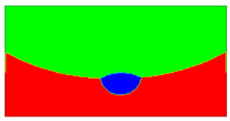	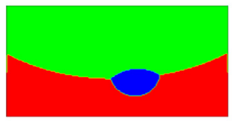
	(c) centroid (102,30)	(c') centroid (104,30)	(c'') centroid (116,32)

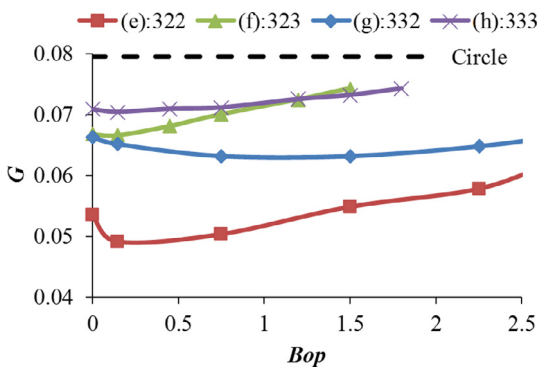

Fig. 13. Relationship between the pseudo bond number and shape factor when $\rho_3 > \rho_1$, "(e):322" denotes $G_{int,12} = 3$, $G_{int,13} = 2$, $G_{int,12} = 2$ in case(e) of Fig. 12.

$G_{ads,1} = -0.5, G_{ads,2} = 0.1, G_{ads,23} = 0.2$ to make the meniscus concave upwards. As the ratio of θ_2 to θ_1 is proportional to the ratio of $G_{int,13}$ to $G_{int,12}$, it can be seen that the larger the ratio of θ_2 to θ_1 is, the faster the droplet moves to the wall and the tendency to move to the wall is more obvious. Similarly, Table 4 shows droplet motion on the concave meniscus when θ_2 is less than θ_1 and the initial centroid of the droplet is (150, 40). It illustrates that the smaller the ratio of θ_2 to θ_1 is, the faster the droplet moves away from the wall and migrates to the center.

To sum up, we have described how control of the droplet shape is implemented in LBM simulations and how the asymmetry of the droplet shape can influence the direction of movement on the meniscus.

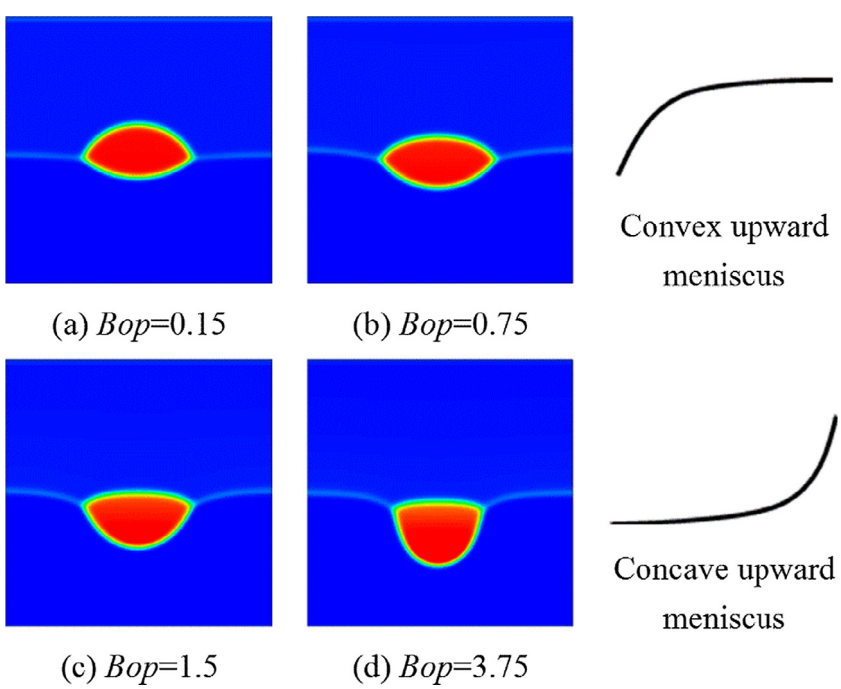

Fig. 14. Density profiles of C_3 at different pseudo bond numbers when $\rho_3 > \rho_1$, $G_{int,12} = 3$, $G_{int,13} = 3$, $G_{int,12} = 2$. A sketch of convex and concave upward meniscus is also given, the deformation of the interface around droplets in such cases generate convex upward menisci.

4.2. Influence of the gravity on the motion

In this section, we regard C_1 and C_2 as liquid and gas phase respectively, thus $k_{21} \equiv 0.001$ in the simulation. And C_3 could be a droplet or a bubble depending on the value of k_{31}.

4.2.1. The cases when $\rho_3 > \rho_1$: water droplets on oil

Let $k_{31} = 1.5$, take the cases (e), (f), (g), and (h) shown in Fig. 12 as basic simulation schemes. Then, by changing the gravitational acceleration g, we can obtain various droplet shapes at different pseudo-Bond numbers. We can define a shape factor $G = A/L^2$ to characterize the droplet, where A is the area of the droplet and L is its perimeter. The shape factor is a parameter that describes the degree of shape regularity. The bigger the shape factor is, the more regular the shape is. The shape factor of the most regular shape, i.e., the circle, is $1/4\pi$. Fig. 13 summarizes the simulation results in terms of shape factor as a function of pseudo-Bond number, and Fig. 14 provides the specific shapes of Case (g) with gravity considered. In Fig. 14, we provide density profiles of C_3 instead of the RGB figures previously shown so that the contact line and surface are smoother. As Fig. 13 shows, the shape factor displays a subtle decrease with increasing pseudo-Bond number at first, and then increases steadily with the pseudo-Bond number, which means that the shape tends to become more and more regular. We can also see from Fig. 14 that the droplet sinks and becomes rounder gradually with increasing pseudo Bond number. Moreover, there is a deformation of the interface around droplets (convex upward meniscus) which is opposite to that near a wetting wall (concave meniscus).

As stated above, gravity would prevent the droplet from moving to the wall when $\rho_3 > \rho_1$. Firstly, gravity makes θ_2 larger and decreases θ_1, and this trend makes the droplet move away from the wall as stated in Section 4.1. Then a convex upward meniscus appears and is opposite to that near a wetting wall. The opposite meniscus could also prevent the tendency to move towards the walls as reported by Vella and Mahadevan, 2005. Last but not least, it is obvious that gravity acts as a resisting force against droplets rising to the wall. Therefore the droplets are more likely to move away from the wall for the cases when $\rho_3 > \rho_1$ except when the pseudo Bond number is extremely small.

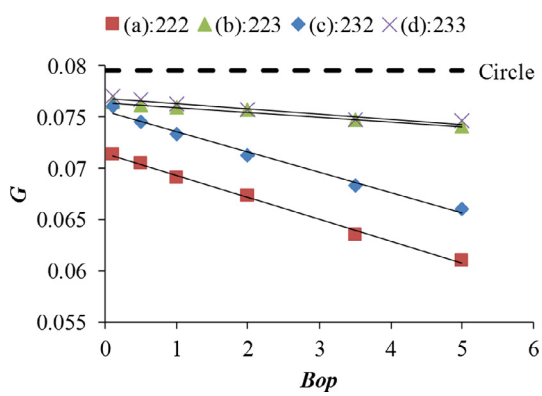

Fig. 15. Relationship between the pseudo bond number and shape factor when $\rho_3 \leq \rho_1$, "(a):222" denotes $G_{int,12} = 2$, $G_{int,13} = 2$, $G_{int,12} = 2$ in case(a) of Fig. 12.

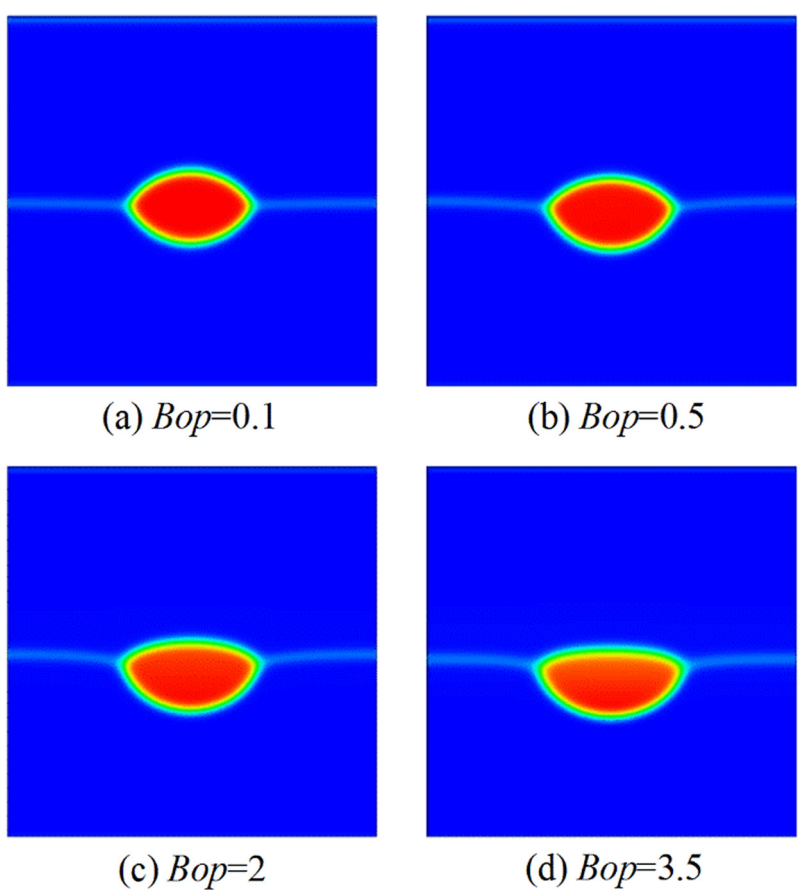

Fig. 16. Density profiles of C_3 at different pseudo-Bond number when $\rho_3 \leq \rho_1$, $G_{int,12} = 2$, $G_{int,13} = 2$, $G_{int,12} = 2$.

4.2.2. The cases when $\rho_3 \le \rho_1$: oil droplets

Let $k_{31} = 0.9$, which means C_3 can be regarded as a fluid such as oil relative to water as C_2, and take the cases (a), (b), (c), and (d) shown in Fig. 12 as basic simulation schemes. We can then change the gravitational acceleration g and get various droplet shapes at different pseudo-Bond numbers. Fig. 15 summarizes simulation results showing the shape factor as a function of pseudo-Bond number, and Fig. 16 provides the specific shapes for Case (a) at different Bond numbers. It can be seen from Fig. 15 that the shape factor declines with increasing pseudo Bond number, which means that the shape tends to become more and more irregular. According to Fig. 16, the droplet tends to extend to both sides with the pseudo-Bond number increasing and the deformation of the interface around droplets (convex upward meniscus) is not as prominent as it was in the $\rho_3 > \rho_1$ case.

Thus, though gravity would prevent the droplet from moving to the wall when $\rho_3 \le \rho_1$, this restraint is not as overwhelming as it is in cases of $\rho_3 > \rho_1$. On one hand, the relatively small ρ_3 leads to a smaller effect of gravity. On the other hand, the curvature of the convex upward meniscus around droplets decreases as well. For example, without gravity the droplet ultimately sticks to the wall in the simulation with $G_{\text{int},12} = 3, G_{\text{int},13} = 3.4, G_{\text{int},23} = 2$ in Table 3. By incorporating the density by setting $k_{21} = 0.001$, $k_{31} = 1.0$, and $g_{LBM} = 3 \times 10^{-5}$ lu/ts^2, we can observe the tendency of the droplet to move when $\rho_3 \le \rho_1$. Fig. 17 shows that the droplet eventually stops on the way to the wall before reaching the wall due to balancing of the opposing forces.

4.2.3. The cases when $\rho_3 \ll \rho_1$: bubbles

By setting $k_{31} = k_{21} = 0.001$, which means that C_2 and C_3 can be regarded as gases relative to a water phase C_1, and taking the cases (e), (f), (g), and (h) shown in Fig. 12 as the basic simulation schemes, we can get various bubble shapes at different pseudo-Bond numbers by changing the gravitational acceleration. Fig. 18 gives information regarding shape factor as a function of pseudo-Bond number, and Fig. 19 provides the specific shapes of Case (f) with the gravity considered. As Fig. 19 shows, the shape factor undergoes a decrease with the pseudo-Bond number increasing, which means that the shape tends to become more and more irregular. We can also see from Fig. 19 that the bubble rises and spreads to both sides gradually with the pseudo-Bond number increasing. The deformation of the interface around the droplet generates concave upward menisci which are the same configurations they assume near a wetting wall.

For $\rho_3 > \rho_1$ and $\rho_3 < \rho_1$ usually the gravity inhabits the bubble motion to the wall. However, gravity would promote the bubble motion to the wall when $\rho_3 \ll \rho_1$. Unlike denser droplets, the downward gravitational force experienced by the bubble is too small to prevent the bubble from rising to the wall. Furthermore, the gravity makes θ_1 larger and decreases θ_2, which can accelerate bubble migration to the wall. In addition, the concave meniscus around the bubble can also provide a driving force. For example, the droplet ultimately moves to the center in the simulation with $G_{\text{int},12} = 3, G_{\text{int},13} = 2, G_{\text{int},23} = 3$ in Table 4. Changing the parameters to $k_{21} = k_{31} = 0.001$, and $g_{LBM} = 3 \times 10^{-4}$ lu/ts^2 shows that the direction of bubble motion is opposite and towards the wall (Fig. 20).

In brief, gravity promotes bubble motion towards a wall while inhibiting droplets from moving to a wall.

4.3. Accelerating the meniscus-induced motion

As stated above, the droplet shape and relative density of a droplet interact with gravity can decide the moving tendency towards the wall. Here we discuss how to accelerate the motion for a certain three phase system, i.e., the interfacial tension and relative density parameters are fixed.

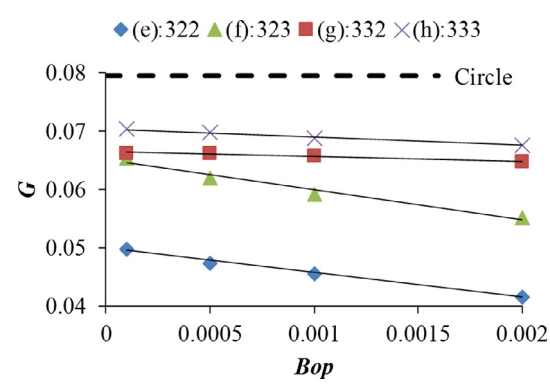

Fig. 18. Relationship between the pseudo bond number and shape factor when $\rho_3 \ll \rho_1$, "(e):322" means the case(e) in Fig. 12 with $G_{\text{int},12} = 3$, $G_{\text{int},13} = 2$, $G_{\text{int},12} = 2$.

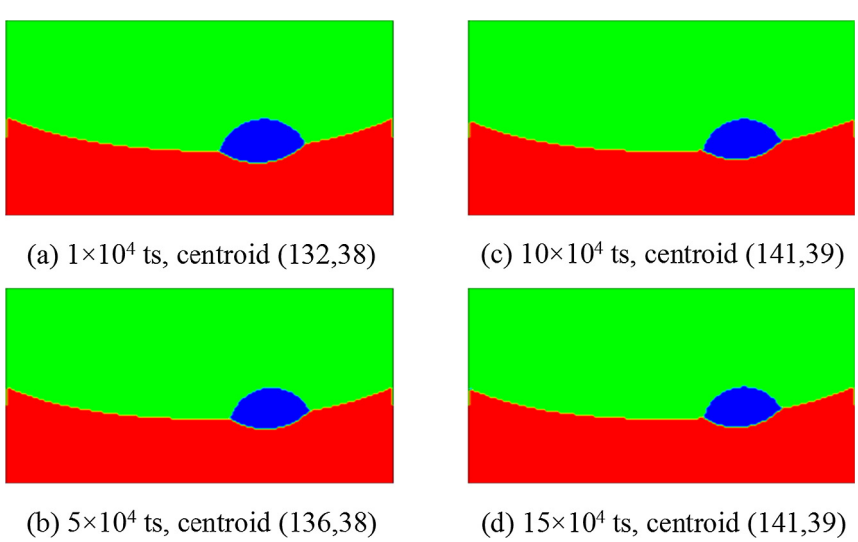

Fig. 17. Gravity prevents the droplet motion from moving to the wall, $\rho_3 \le \rho_1$, $G_{\text{int},12} = 3$, $G_{\text{int},13} = 3.4$, $G_{\text{int},12} = 2$ and $g_{\text{LBM}} = 3 \times 10^{-5}$ lu/ts^2.

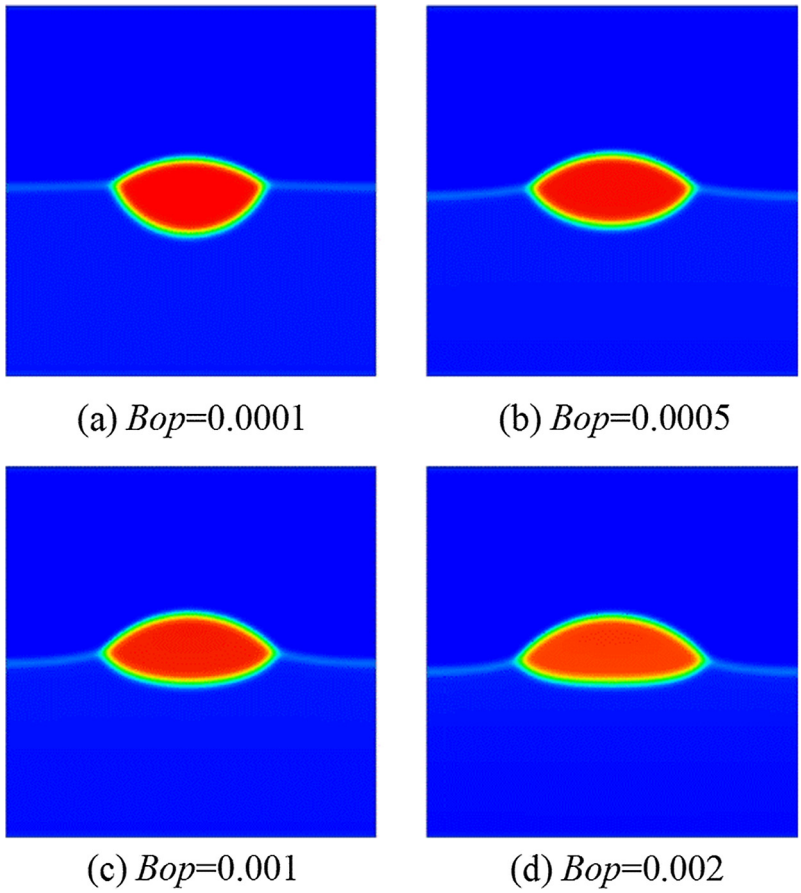

Fig. 19. Density profiles of C_3 at different pseudo bond number when $\rho_3 \ll \rho_1$, $G_{int,12}$ = 3, $G_{int,13}$ = 3.4, $G_{int,12}$ = 2.

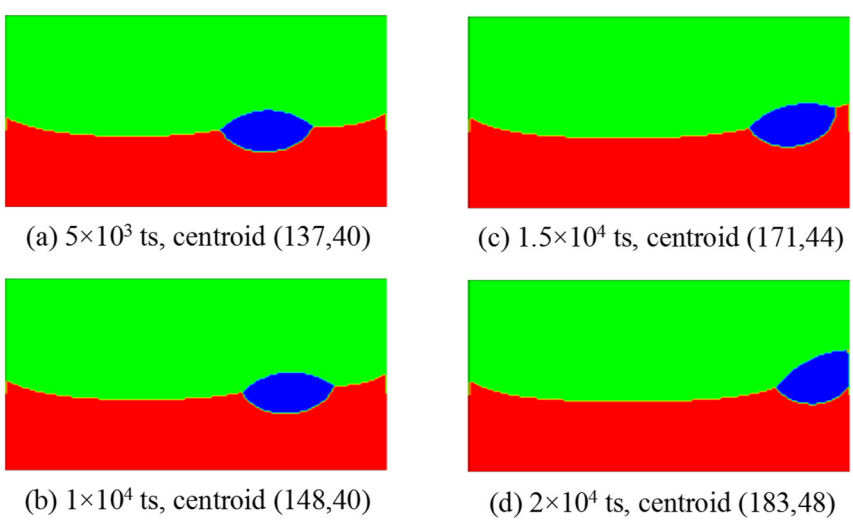

Fig. 20. Gravity promotes the bubble motion towards the wall, $\rho_3 \ll \rho_1$, $G_{int,12}$ = 3, $G_{int,13}$ = 2, $G_{int,12}$ = 3 and g_{LBM} = 3 × 10^{-4} lu/ts^2.

4.3.1. Influence of the droplet size

Using the simulation when $G_{int,12} = 3, G_{int,13} = 3, G_{int,23} = 2$ in Table 3 as the basic scheme, the influence of droplet size is investigated through calculating the velocities based on the centroid coordinate. It is seen from Fig. 21 that the smaller the droplet, the faster it moves. In general, the velocity increases during the migration to the wall, due to steepening of the meniscus during migration to a wall. Based on these results, a possible way to enhance the motion is breaking large droplets into smaller ones.

4.3.2. Influence of the meniscus curvature

We again use the simulation where $G_{int,12} = 3, G_{int,13} = 3, G_{int,23} = 2$ in Table 3 as the basic scheme, and set the droplet size at 12 lu. Changing $G_{ads,1}$, and $G_{ads,2}$ to create different menisci and then calculating the velocities during the motion towards the wall permits assessment of the influence of the contact angle. Here we use the contact angle between the meniscus and the wall to characterize the meniscus curvature. The results are shown in Fig. 22. It is obvious that larger curvature generally leads to higher speed.

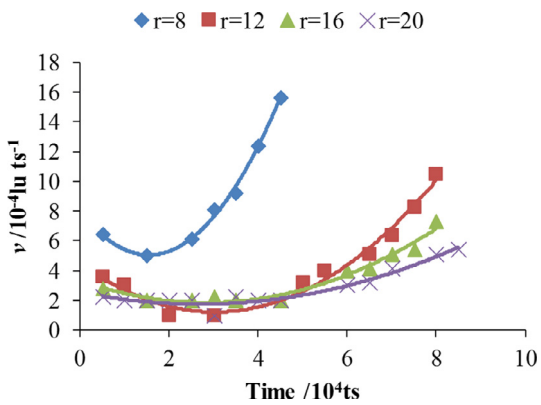

Fig. 21. Influence of droplet size on velocity.

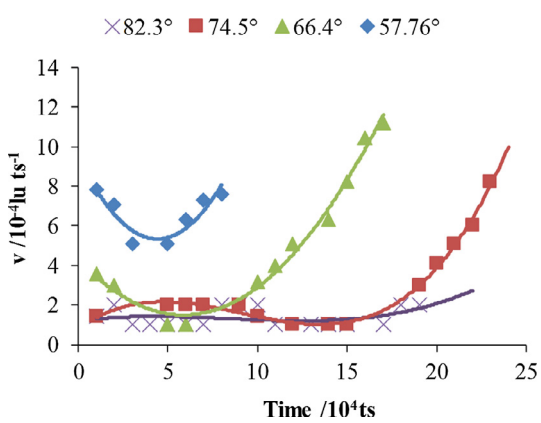

Fig. 22. Influence of the meniscus curvature on velocity, the contact angle between the meniscus and the wall is used to characterize the meniscus curvature.

Slightly elevated initial velocities are likely due to model adjustment to initial conditions. For the highest contact angle (82.3°, the lowest meniscus curvature), the meniscus is nearly flat and the droplet motion is retarded. Thus we can enhance the motion by changing the wall wettability. They non-monotonicity of the velocities in time suggests there are more complex fluid dynamics and/or model start-up factors affecting the droplet motion.

5. Conclusion

In this paper, a three phase MCMP LBM model has been verified against theory and experimental data. Based on the model, the meniscus-induced motion of droplets and bubbles is studied.

To begin with, a method to control the contact angle of droplets on the interface is provided in the three fluid phase Lattice Boltzmann model. The main idea is to adjust interaction force parameters based on the force balance model.

Then we find that the symmetry characteristics of droplet shape influence the tendency for droplets to move towards a wall. Droplets tend to move to the wall on a concave upwards meniscus when they have a big "head" and a small "belly" as controlled by the interfacial tensions. Otherwise droplet tend to move away from a wall.

Gravity influences the spontaneous motion in three ways, i.e., changing the droplet shape, triggering a deformation of the interface around a droplet, and itself acting as a force contributing to the motion. The gravity only promotes the motion towards the wall when the density of the droplet is relatively small, such as when the droplet is a low-density bubble.

Finally, smaller droplet size and larger meniscus curvatures accelerate the trend for spontaneous movement towards a wall. These observations provide a way to enhance the motion of droplets by diminishing their size and increasing the meniscus curvature. In addition, droplets accelerate during migration to a wall due to steepening of the meniscus.

Acknowledgements

Hou and Wei greatly appreciate the financial support of the National Natural Science Foundation of China (Grant no. 51574269), the National Science Foundation for Distinguished Young Scholars of China (Grant No. 51625403), the Important National Science and Technology Specific Projects of China (Grant no. 2016ZX05011-003), the Fundamental Research Funds for the Central Universities (Grant no. 15CX08004A, 13CX05007A, 14CX05025A, 15CX06025A), the Innovation program for graduates of China University of Petroleum (Grant no. YCXJ2016022). Huang is supported by National Natural Science Foundation of China (Grant no. 11472269). For Sukop, this material is based upon work supported by the National Science Foundation under Grant No. EAR-1204762. Wei also is supported by China Scholarship Council.

Appendix A. Supplementary material

Supplementary data associated with this article can be found, in the online version, at https://doi.org/10.1016/j.ces.2017.10.025.

Reference

Alheshibri, M.H., Rogers, N.G., Sommers, A.D., Eid, K.F., 2013. Spontaneous movement of water droplets on patterned Cu and Al surfaces with wedge-shaped gradients. Appl. Phys. Lett. 102 (17), 174103.
Bao, J., Schaefer, L., 2013. Lattice Boltzmann equation model for multi-component multi-phase flow with high density ratios. Appl. Math. Model 37 (4), 1860–1871.
Bhatnagar, P.L., Gross, E.P., Krook, M., 1954. A model for collision processes in gases. I. small amplitude processes in charged and neutral one-component systems. Phys. Rev. 94 (3), 511.
Celestini, F., Frisch, T., Pomeau, Y., 2013. Take off of small leidenfrost droplets. Phys. Rev. Lett. 109 (3), 034501.
Chen, S., Yuan, X., Fu, B., Yu, K., 2011. Simulation of interfacial marangoni convection in gas-liquid mass transfer by Lattice Boltzmann method. Front. Chem. Sci. Eng. 5 (4), 448–454.
Chen, Y., Kang, Q.J., Cai, Q., Wang, M., Zhang, D., 2015. Lattice Boltzmann simulation of particle motion in binary immiscible fluids. Commun. Comput. Phys. 18 (3), 757–786.
Chen, Y.F., Chen, H.Y., Sheng, Y.J., Tsao, H.K., 2017. Directed drift and fluid pumping of nanoswimmers by periodic rectification-diffusion. J. Chem. Phys. 146 (1), 014902.
Corneli, J., Holt, P., Lee, G., Leger, N., Schoenfeld, E., Steinhurst, B., 2004. The double bubble problem on the flat two-torus. Trans. Am. Math. Soc. 356 (9), 3769–3820.
Fournier, J.B., Cazabat, A.M., 1992. Tears of wine. Europhys. Lett. 20 (6), 517.
Fu, Y., Zhao, S., Bai, L., Jin, Y., Cheng, Y., 2016. Numerical study of double emulsion formation in microchannels by a ternary Lattice Boltzmann method. Chem. Eng. Sci. 146, 126–134.
Gascoyne, P.R., Vykoukal, J.V., Schwartz, J.A., Anderson, T.J., Vykoukal, D.M., Current, K.W., McConaghy, C., Becker, F.F., Andrews, C., 2004. Dielectrophoresis-based programmable fluidic processors. Lab Chip 4 (4), 299–309.
Genzer, J., 2012. Surface-bound gradients for studies of soft materials behavior. Annu. Rev. Mater. Res. 42, 435–468.
Gillard, M., Sutcliffe, P., 2009. Domain walls and double bubbles. In: Proceedings of the Royal Society of London A: Mathematical, Physical and Engineering Sciences. The Royal Society (p. rspa20090227).
Guo, Z., Shu, C., 2013. Lattice Boltzmann Method and Its Applications in Engineering, vol. 3. World Scientific, pp. 66–76.
Hernandez, S.C., Bennett, C.J., Junkermeier, C.E., Tsoi, S.D., Bezares, F.J., Stine, R., Robinson, J.T., Lock, E.H., Boris, D.R., Pate, B.D., Caldwell, J.D., Reinecke, T.L., Sheehan, P.E., Walton, S.G., 2013. Chemical gradients on graphene to drive droplet motion. ACS Nano 7 (6), 4746–4755.
Hilner, E., Zakharov, A.A., Schulte, K., Kratzer, P., Andersen, J.N., Lundgren, E., Mikkelsen, A., 2009. Ordering of the nanoscale step morphology as a mechanism for droplet self-propulsion. Nano Lett. 9 (7), 2710–2714.
Hou, Y., Gao, L., Feng, S., Chen, Y., Xue, Y., Jiang, L., Zheng, Y., 2013. Temperature-triggered directional motion of tiny water droplets on bioinspired fibers in humidity. Chem. Commun. 49 (46), 5253–5255.

Huang, H., Sukop, M.C., and Lu, X., first ed., 2015. Multiphase Lattice Boltzmann Methods: Theory and Application. John Wiley & Sons.
Huang, H., Thorne Jr, D.T., Schaap, M.G., Sukop, M.C., 2007. Proposed approximation for contact angles in Shan-and-Chen-type multicomponent multiphase Lattice Boltzmann models. Phys. Rev. E 76 (6), 066701.
Joanny, J.F., Jülicher, F., Prost, J., 2003. Motion of an adhesive gel in a swelling gradient: a mechanism for cell locomotion. Phys. Rev. Lett. 90 (16), 168102.
Joshi, A.S., Sun, Y., 2009. Multiphase Lattice Boltzmann method for particle suspensions. Phys. Rev. E 79 (6), 066703.
Leclaire, S., Reggio, M., Trépanier, J.Y., 2013. Progress and investigation on lattice Boltzmann modeling of multiple immiscible fluids or components with variable density and viscosity ratios. J. Comput. Phys. 246, 318–342.
Li, Q., Kang, Q.J., Francois, M.M., Hu, A.J., 2016. Lattice Boltzmann modeling of self-propelled leidenfrost droplets on ratchet surfaces. Soft Matter 12 (1), 302–312.
Li, Q., Luo, K.H., 2013. Achieving tunable surface tension in the pseudopotential lattice Boltzmann modeling of multiphase flows. Phys. Rev. E 88 (5), 053307.
Li, S., Liu, J., Hou, J., Zhang, G., 2015. Meniscus-induced motion of oil droplets. Colloids Surf. A 469, 252–255.
Liu, J., Li, S., Hou, J., 2016. Near-post meniscus-induced migration and assembly of bubbles. Soft Matter 12 (7), 2221–2230.
Lv, C., Chen, C., Chuang, Y.C., Tseng, F.G., Yin, Y., Grey, F., Zheng, Q., 2014. Substrate curvature gradient drives rapid droplet motion. Phys. Rev. Lett. 113 (2), 026101.
Martys, N.S., Chen, H., 1996. Simulation of multicomponent fluids in complex three-dimensional geometries by the lattice Boltzmann method. Phys. Rev. E 53 (1), 743.
Matsushita, S., Tanaka, S., Yoshida, K., Kobayashi, K., Tsuruki, Y., Shibuya, Y., Isobe, T., Nakajima, A., 2012. Activation of the spontaneous motion of a nitrobenzene droplet by chlorobenzene blending. Colloids Surf. A 395, 233–239.
Nakata, S., Iguchi, Y., Ose, S., Kuboyama, M., Ishii, T., Yoshikawa, K., 1997. Self-rotation of a camphor scraping on water: new insight into the old problem. Langmuir 13 (16), 4454–4458.
Ngachin, M., Galdamez, R.G., Gokaltun, S., Sukop, M.C., 2015. Lattice Boltzmann simulation of rising bubble dynamics using an effective buoyancy method. Int. J. Mod. Phys. C 26 (03), 1550031.
Nguyen, N.T., Ng, K.M., Huang, X., 2006. Manipulation of ferrofluid droplets using planar coils. Appl. Phys. Lett. 89 (5), 052509.
Oshima, S., Nomoto, T., Toyota, T., Fujinami, M., 2014. Surface tension gradient around an alcohol droplet moving spontaneously on a water surface. Anal. Sci 30, 441–444.
Qian, Y.H., d'Humières, D., Lallemand, P., 1992. Lattice BGK models for Navier-Stokes equation. Europhys. Lett. 17 (6), 479.
Ren, F., Song, B., Sukop, M.C., 2016. Terminal shape and velocity of a rising bubble by phase-field-based incompressible Lattice Boltzmann model. Adv. Water Resour. 97, 100–109.
Rybalko, S., Magome, N., Yoshikawa, K., 2004. Forward and backward laser-guided motion of an oil droplet. Phys. Rev. E 70 (4), 046301.
Sbragaglia, M., Belardinelli, D., 2013. Interaction pressure tensor for a class of multicomponent lattice Boltzmann models. Phys. Rev. E 88 (1), 013306.
Semprebon, C., Krüger, T., Kusumaatmaja, H., 2016. Ternary free-energy lattice Boltzmann model with tunable surface tensions and contact angles. Phys. Rev. E 93 (3), 033305.
Sega, M., Sbragaglia, M., Kantorovich, S.S., Ivanov, A.O., 2013. Mesoscale structures at complex fluid–fluid interfaces: a novel lattice Boltzmann/molecular dynamics coupling. Soft Matter 9 (42), 10092–10107.
Shan, X., Chen, H., 1993. Lattice Boltzmann model for simulating flows with multiple phases and components. Phys. Rev. E 47 (3), 1815.
Shan, X., Chen, H., 1994. Simulation of nonideal gases and liquid-gas phase transitions by the lattice Boltzmann equation. Phys. Rev. E 49 (4), 2941.
Shum, H., Tripathi, A., Yeomans, J.M., Balazs, A.C., 2013. Active ciliated surfaces expel model swimmers. Langmuir 29 (41), 12770–12776.
Sukop, M.C., Thorne Jr, D.T., second ed., 2006. Lattice Boltzmann Modeling, Springer.
Sumino, Y., Magome, N., Hamada, T., Yoshikawa, K., 2005. Self-running droplet: emergence of regular motion from nonequilibrium noise. Phys. Rev. Lett. 94 (6), 068301.
Sun, C., Zhao, X.W., Han, Y.H., Gu, Z.Z., 2008. Control of water droplet motion by alteration of roughness gradient on silicon wafer by laser surface treatment. Thin Solid Films 516 (12), 4059–4063.
Taylor, J.E., 1976. The structure of singularities in soap-bubble-like and soap-film-like minimal surfaces. Ann. Math., 489–539
Van Kats, F.M., Egberts, P.J.P., 1999. Simulation of three-phase displacement mechanisms using a 2D lattice-Boltzmann model. Transp. Porous Media 37 (1), 55–68.
Vella, D., Mahadevan, L., 2005. The "cheerios effect". Am. J. Phys. 73 (9), 817–825.
Wang, L., Yuan, B., Lu, J., Tan, S., Liu, F., Yu, L., He, Z., Liu, J., 2016. Self-propelled and long-time transport motion of PVC particles on a water surface. Adv. Mater. 28 (21), 4065–4070.
Woog Lee, D., Jin Im, D., Kang, I.S., 2012. Electrophoretic motion of a charged water droplet near an oil-air interface. Appl. Phys. Lett. 100 (22), 221602.
Xu, X., Qian, T., 2012. Droplet motion in one-component fluids on solid substrates with wettability gradients. Phys. Rev. E 85 (5), 051601.
Yao, L., Sharifi-Mood, N., Liu, I.B., Stebe, K.J., 2015. Capillary migration of microdisks on curved interfaces. J. Colloid Interface Sci. 449, 436–442.